International Journal of Aviation Science and Technology

*Research Article*

# Numerical Aerodynamic and Aeroacoustic Analysis of Toroidal Propeller Designs

Xuan-Duc Vu[1], Anh-Tuan Nguyen[2], Tuong-Linh Nha[3], Hoang-Quan Chu[4], Cong-Truong Dinh[5]*

[1] *School of Mechanical Engineering, Hanoi University of Science and Technology, Hanoi 11615, Vietnam*
*duc.vx196848@sis.hust.edu.vn* - 0009-0003-5788-5233
[2] *School of Mechanical Engineering, Hanoi University of Science and Technology, Hanoi 11615, Vietnam*
*tuan.nguyenanh@hust.edu.vn* - 0009-0001-5057-5289
[3] *School of Mechanical Engineering, Hanoi University of Science and Technology, Hanoi 11615, Vietnam*
*linh.nhatuong@hust.edu.vn* - 0009-0006-6975-5075
[4] *Faculty of Aerospace Engineering, Le Quy Don Technical University, Hanoi 11917, Vietnam*
*chu.h-quan.fas@lqdtu.edu.vn* - 0000-0002-9312-0508
[5] *School of Mechanical Engineering, Hanoi University of Science and Technology, Hanoi 11615, Vietnam*
*truong.dinhcong@hust.edu.vn* - 0000-0001-5357-1534

## Abstract

Drones have a major drawback which prevents them from being used extensively - the excessive noise they produce. This article presents an optimization process of aerodynamic noise reduction for a novel design called the Toroidal Propeller, which consists of two blades looping joined in a manner where the end of one blade arches back into the other, has been designed by the Aerospace Propulsion Systems (APSs) research team at School of Mechanical Engineering, Hanoi University of Science and Technology. In addition, four toroidal propellers with different curved shapes (pitch) and Number of Blades (NOB) are considered. The goal of this research is to evaluate the effects of modifying the geometry design of the Toroidal Propeller on the intensity of blade tip vortex and aerodynamic flow characteristics passing through the blade. The ultimate goal is to decrease blade tip vortex and turbulence produced by the blade, which can help estimate the sound pressure level and minimize it without causing significant performance losses. Based on the outcome results, the models of the four geometry studies are compared in terms of Acoustic Power Level (APL), Surface Acoustic Power Level (SAPL), Thrust, Torque, and Power. In general, the propeller model with NOB of 3 provides the most optimal efficiency in terms of both Thrust and APL. At the output cross-section, the APL dropped from nearly 139 dB to 121 dB, while thrust increased from almost 6.2N to 8.7N compared to the first version of the Toroidal Propeller model.

## Keywords

Toroidal Propeller
Blade Number
Thrust
Acoustic Power Level
Surface Acoustic Power Level

## Time Scale of Article

Received 21 December 2023
Revised until 27 March 2024
Accepted 1 April 2024
Online date 21 June 2024

## 1. Introduction

Unmanned aerial vehicles (UAVs) have become increasingly useful in both military and civil applications over the past few years. Among the various vehicle power configurations, rotary-wing vehicles with vertical take-off and landing abilities remain popular, while propellers are the most commonly used. The propeller is a key component of a rotorcraft, providing the necessary

*: Corresponding Author Cong-truong Dinh, truong.dinhcong@hust.edu.vn
DOI: 10.23890/IJAST.vm05is01.0102

propulsion to enable aircraft movement (Dantsker, O.D., 2022). Drones are small, remote-controlled aircraft used for services like package delivery, aerial photography, and more. They're cost-effective, eco-friendly, and can navigate tight spaces where humans can't go. In 2017, the psychoacoustic experiments were conducted by NASA Langley Research Center, the findings indicate that humans are more responsive to the noise generated by small multirotor drones than to noise from other forms of traffic (Krishnamurthy, S., 2021). This finding suggests that the use of quieter propellers could potentially accelerate the public's acceptance and commercial adoption of drones. Since drones are often heard before they are seen, it is important to reduce their sound footprint to make them less detectable. The engine and propeller of the UAVs contribute the most to the noise and reducing the noise of propellers is a challenging task as the designs that produce less noise can have reduced efficiency. Designing quiet propellers is an area of active research. Some studies have explored ways to decrease propeller noise (Gur and Rosen, 2009; Wu et al., 2019; Chirico et al., 2018; Wisniewski et al., 2015; Wisniewski et al., 2015; Demoret and Wisniewski, 2019; Wisniewski and Van Treuren, 2022; Axel Schulz, 2023).

Gur and Rosen (2009) focused on utilizing a silent propeller on a mini-UAV using electrical power. The study conducted by the researchers provided valuable insights into the factors affecting the performance and noise generated by the propeller. By analyzing blade shape, cone angle, diameter, speed, and NOB, they discovered that increasing NOB significantly makes the propeller quieter.

Wu et al. (2019) conducted a study on propeller noise and it was found that the loudest noise is produced at the blade tip. They employed numerical techniques to explore how propeller geometry and rotational speed can help the development of design a quieter propeller. The study revealed that the noise generated by a propeller is made up of a low-frequency sound that remains constant and high-frequency sounds that occur at specific points throughout the operation of the propeller. With increasing revolutions per minute, the high-frequency sounds become more prominent. To reduce the noise, the researchers altered the blade geometry along the spanwise direction while the blade width was expanded in a radial direction. According to a study by Chirico et al. (2018), the application of computational fluid dynamics (CFD) can be instrumental in the estimation of APL and noise spectra for different blade shapes and hub geometries. According to the research findings, designing a blade that operates at slow speed rotation and features inboard migration of spanwise loading is deemed to be extremely quiet and isn't causing notable disadvantages.

The efficacy of various combinations of radius, pitch, and NOB on aerodynamic efficiency and APL have been studied by Wisniewski et al. (2015) through experimental investigations. They identified the ideal pitch in which the APL is minimized. The results also revealed that the noise generated was heavily dependent on the propeller's rotational speed. The research also by Wisniewski and colleagues (2015) conducted a study to investigate how propeller performance and noise are affected by aerofoil shape and tip configuration. The study included four airfoils, with the GM15 airfoil emerging as the top performer for two-bladed propellers. The study also found that propellers with Oval tips outperformed those with round, tapered, or flat tips. Based on these findings, a hybrid propeller was developed to achieve optimal performance by combining the GM15 airfoil with an Oval tip. According to a study by Demoret and Wisniewski (2019), the principal cause of propeller noise is blade-tip vortices. To mitigate this issue, they suggested that the blade-tip rotational speed or vortex strength be decreased. Recently, research conducted by Wisniewski and Van Treuren (2022) explored new designs of propellers that have less thrust-load at the blade-tip. This can be attributed to the reduction in the vortex strength of the blade-tip, which resulted in a decrease in the level of sound pressure and the necessary power.

Axel Schulz (2023) has studied the impact of modifying the trailing edge of a drone propeller manufactured by APC Propellers. The results from the simulations show that a modification can reduce the tonal noise caused by the vortex feedback mechanism between leading edge (LE) and trailing edge (TE) as well as the overall sound level in the broadband component of the noise. However, a modification where the material is removed results in a reduction of propeller lift force. The place of the modification seems to play a big role in the overall sound characteristic of the propeller. The best-performing propeller had a sinusoidal cutaway along the entire TE.

The objective of this project is to analyze the impact of modifying the blade shape and wing-tip configurations to decrease the intensity of wing-tip vortices, minimize turbulence in the flow across the blade and, as a result, reduce the noise generated by the propeller. This article is also mainly focused on examining computational methods for predicting propeller performance and acoustic power levels. During the simulations, the propeller's rotational speed is tested at varying minimum to maximum speeds. The data collected from these simulations are used to compare the thrust and torque produced. The propellers are set to rotate at a consistent and unchanging rate of speed in the second simulation, and the corresponding APL and SAPL values are estimated from the collected data.

The recent research conducted by MIT University

Cambridge on the toroidal propeller is certainly an interesting development for the drone industry. The researchers claim that these propellers produce less high pitch noise compared to traditional propellers, without any loss in efficiency (MIT Lincoln Laboratory, 2022; Sebastian, T. and Strem, C., 2020). If proven successful, the use of toroidal propellers could revolutionize the drone industry. For decades, researchers and companies have been studying and developing the concept of Ring Wings, which involves rotating an airfoil in a toroidal shape. This idea eventually led to the development of various propellers used today. This concept was found to reduce noise and increase efficiency, and many researchers and marine companies continued to build on it. This design was patented in the 1980s without much discussion, but recent MIT experiments have renewed interest in its propeller design, opening up new possibilities for its utilization.

The MIT toroidal propeller design features a pair of interlocking blades. Specifically, the two blades cleverly intertwine in a manner whereby the tip of one curve back into the other, reducing drag from swirling air tunnels (vortices) at their tips and improves the overall stiffness of the propeller, which helps to reduce the noise. The propeller's toroidal shape helps minimize blade-tip vortex by constraining the flow and controlling spillover of the edges. The number of blades and pitch also affect noise and vibration. Due to the blade's curved shape and the non-linear relationship between blade angle and performance, establishing the pitch in toroidal propellers is a complex process. The key features of this Toroidal propeller have been outlined by MIT which include: lowers the signals in the frequency range that humans are most sensitive to; without the need for additional components, it reduces noise and avoids adding weight or consuming power; reduces the chances of the rotating propeller will coming into contact with objects or surfaces in the drone's trajectory, minimizing the risk of cutting, catching, or clipping; Reliably manufacture this using additive techniques to produce thrust similar to a multirotor drone propeller, which enables the customization of the propeller for different models and types of multirotor. Tests conducted on commercial quadcopters using toroidal propellers have shown in Fig.1 that they can produce thrust levels comparable to conventional propellers at similar power levels. These propellers produce reduced noise levels, allowing drones to operate without harming human hearing at half the distance.

The article is structured in the following way: firstly, it reviews the methods used for aero-acoustic modeling. Secondly, it describes the test cases, followed by an explanation of the computational grids, the flow solver, and the computational setup. Thirdly, it presents the results and discusses them. Lastly, the article provides concluding remarks.

## 2. Aerodynamic Characteristics of Propellers

The traditional design of propellers typically comprises radiating blades and rotating hub. The blades are angled at a specific pitch to create a helical shape and rotate around the hub. The propeller causes forward motion by using its blades to push against air, powered by the engine or motor (Gerr, D., 1989). Nevertheless, the amount of the thrust produced by a propeller is not always constant and depends on factors such as the propeller's rotational and incoming flow velocities. Hence, tests conducted on propellers often involve examining their performance under a variety of operating conditions (Vargas Loureiro, E. et al., 2021). To optimize rotorcraft performance and energy efficiency, consider propeller variations and aerodynamic parameters. The propeller's performance is evaluated based on normalized coefficients such as efficiency (η), power coefficient (CP), and the thrust coefficient (CT), which can be calculated using equations (1) from Ref. (Seddon, J. and Newman, S., 2011):

$$C_T = \frac{T}{\rho n^2 D^4}, C_P = \frac{P}{\rho n^3 D^5}, \eta = \frac{TV}{P} \quad (1)$$

where P and T represent power (W) and the thrust (N), respectively. $D$, $n$, $\rho$, *and* V represent propeller diameter (m), rotational velocity (rev/s), air density (kg/m$^3$), and the forward speed of a vehicle propelled by a propeller (m/s), respectively. As velocity (V) approaches zero, propeller efficiency (η) also approaches zero, and propeller thrust becomes the static thrust (T).

## 3. Aero-Acoustic Modeling Methods

The propeller noise is comprised of two main components: vortex (broadband) and rotational (tones) noise. Broadband noise, commonly known as vortex noise, is generated due to the presence of blade-tip and LE vortices, free-stream turbulence, and separated flows.

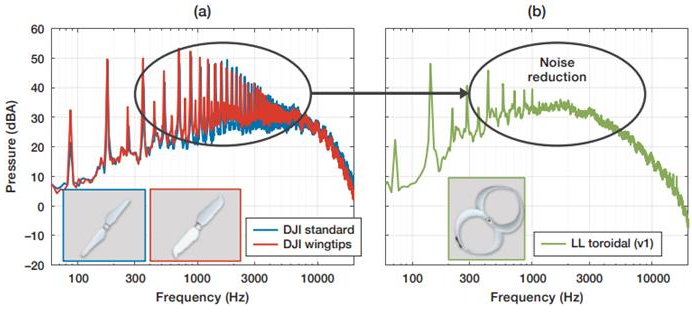


**Fig. 1.** The toroidal propeller (b) used on DJI's quadrotors in comparison to the conventional propellers (a) shows a noteworthy decrease in noise produced by the toroidal propeller.

Rotating blades induce a velocity gradient from the hub to the tip, resulting in a broad range of shedding frequencies associated with vortex shedding. The strength of shedding vortices is directly proportional to the vortex noise, and the noise is mainly caused by the tip frequency, as it is related to the velocity of the section to the sixth power.

All sounds that are related to the harmonics of the blade passage frequency are referred to as rotational noise. As the harmonic order increases, the sound pressure level decreases. Any irregularities in the blade geometry and/or the blade spacing in the azimuthal direction can result in additional sub-harmonics in the noise spectrum (Chirico et al., 2018). Chirico et al. (2018), state that subsonic wing-tip rotation produces two types of noise: monopole due to blade thickness and dipole due to aerodynamic load variations on the blade. When blade-tip Mach numbers range from approximately 0.6 to 0.7, the loading noise predominates. However, as Mach numbers increase, the thickness noise becomes more prominent. The propeller thrust and torque create rotational noise, which increases with larger diameter or fewer blade numbers. The source of the noise diminishes as the distance from it increases in a manner that varies inversely with the square of the distance (Roskam, J. and Lan, C., 1997).

Methods for estimating propeller rotational and vortex noise were introduced by Made and Kurtz in their study (Marte, J.E. and Kurtz, D.W., 1970). When it comes to conventional propellers with moderate forward velocities and tip speeds, the estimation of rotational noise can be achieved by:

$$p_{rms} = \frac{169.3 \cdot m \cdot B \cdot R \cdot M_t}{S \cdot A}\left[\frac{0.76 \cdot P_h}{M_t^2 - T \cdot \cos\theta}\right] \cdot J_{mb}(x) \qquad (2)$$

where:

$p_{rms}$ = rms APL in dynes/cm$^2$

S = distance from propeller hub to observer, ft

Ph = absorbed power, horsepower

X = The Bessel function's argument, 0.8MtmB sinθ

Θ = angle from forward propeller axis to observer

B = NOB

M = harmonic's orders

R = propeller radius, ft

A = propeller disc area, ft2

Mt = tip Mach number

T = thrust, lb

This formula shows that the amount of noise rises as the absorbed power and diameter increase, the number of blades decreases, particularly when the tip speed is increased. The APL of the noise's vortex produced by traditional propellers can be approximated by this formula:

$$SPL = 10 \cdot log \frac{k \cdot A_b \cdot (V_{0.7})^6}{10^{-16}} \qquad (3)$$

where:

k =the proportionality constant;

$V_{0.7}$ = velocity at 0.7 radius

Ab = the area of blade, ft$^2$

The equation demonstrates that the noise caused by the vortex is heavily dependent on the speed of the blade. Increasing the blade velocity by two times results in an 18 dB increase in SPL. It's important to note that decreasing the blade velocity will affect the propeller's performance. An alternative solution is to decrease the vortex strength represented by $C_L$, the lift coefficient, in the equation below.

$$SPL = 10 \cdot log \frac{6.1 \cdot 10^{-27} \cdot A_b \cdot (V_{0.7})^6}{10^{-16}} + 20 \cdot log \frac{C_L}{0.4} \qquad (4)$$

One way to decrease propeller vortex noise is by lessening the intensity of the tip vortex. This can be achieved by decreasing lift production near the tips of the propeller.

## 4. Description of Numerical Methods

CFD models are utilized to replicate 3D flows that are time-dependent, incompressible, and viscous by applying the Navier-Stokes equations of momentum and mass conservation through discrete techniques (Stokkermans et al., 2019; Klimchenko and Baeder, 2020; Stuermer, 2008).

In this study, commercially available software called ANSYS-FLUENT 2019 R1 is used to conduct RANS-based simulations.

(a) (b)

**Fig. 2.** 3D Toroidal Propeller models (a) Bi-loop Toroidal Propeller version 1-2-3 (b) Tri-loop Toroidal Propeller

In the beginning, the model geometry of the Bi-loop Toroidal Propeller is created in Fusion 360 by using the MIT Toroidal Propeller as a citation, the geometric framework of the Tri-loop Toroidal Propeller also created, are shown in Fig. 2, which is then imported to ANSYS. This part provides further details about how to develop the CFD model. It covers aspects such as defining the computational region, conditions at its boundaries, creating the mesh, and assessing its quality, as well as configuring the solver parameters.

### 4.1 Boundary Conditions and Computational Domain

Fig.3 displays a diagram outlining the numerical region and conditions at its boundaries. In order to implement the multiple reference frame (MRF) model, the division of the computational domain results in two distinct zones: an internal rotating fluid zone (Rotation-Domain) and an external stationary fluid zone (Fluid-Domain). The cylindrical shape of a stationary fluid zone is employed to mimic a significant portion of the surrounding air to create a realistic simulation. This setup is in line with several previous research (Stokkermans et al., 2020; Kim, D. et al., 2021; Li, Y. et al., 2023). It is possible to select a domain that is sufficiently extensive to avoid affecting the results. The stationary fluid zone has a length of 22D and a diameter of 11D. It represents the area where the fluid remains still. The flow field near the propeller is depicted by a cylindrical rotating fluid zone that has a length of 0.4D and a diameter of 1.1D. The geometric center of the rotating region is positioned at 25mm from the inlet side and 20mm from the outlet side. The propeller model is situated within the rotating fluid zone, which moves with the same rotor rotational speed. There are two interfaces present at the interface where the stationary and rotating fluid zones meet. The interface in the rotating fluid zone is referred to as Interface 1, while the other is called Interface 2 (Liu, X. et al., 2022; Gómez-Iradi, S., 2009).

About the boundary conditions, the inlet face of the region of fluid that remains stationary is specified as a pressure inlet. However, no information has been provided on the turbulence intensity and viscosity ratio of the test case.

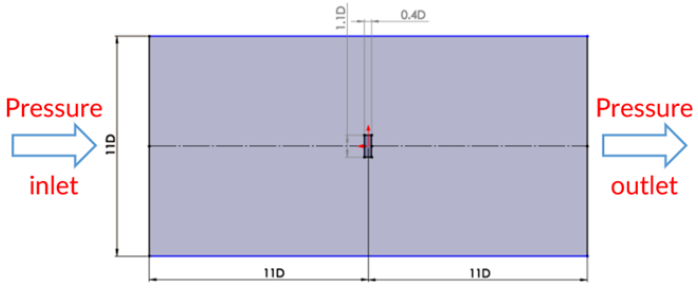


**Fig. 3.** Computational domain

According to the FLUENT user manual (2019), a turbulence intensity of 5% and a viscosity ratio of 10 have been selected. This selection has been made because the case is an open flow.

The working fluid has a constant density of 1.225 kg/m$^3$ and viscosity of 1.7894e-05 kg/m.s. The pressure outlet with a static pressure of 0 Pa is defined as the outlet boundary condition. The pressure difference is set to zero as the outlet flows into a continuous free-stream. The four remaining faces are defined as free-slip walls, while the no-slip wall, that surrounds the rotating fluid zone is set as the rotor surface. To prevent any flow through the wall and create a boundary layer, the propeller is subjected to a wall boundary condition, which is set to a no-slip wall. Since the roughness is unknown, the constant is set to 0.5. The objective of these configurations is to simulate a conventional operation environment. The stationary and rotating regions' geometric boundaries are simulated based on several prior CFD analyses (Vargas Loureiro, E. et al., 2021; Garofano-Soldado, A., 2022; Céspedes M., J.F. and Lopez M., O.D., 2019). The sides of the domain have a symmetry boundary condition since the flow is uniform in this area. Since the symmetry boundary condition is far away from the propeller, it should remain unaffected by it and maintain its free-stream properties.

### 4.2 Mesh Generation and Evaluation

Since the computational domain is partitioned into two zones: the Fluid-Domain and the Rotation-Domain, two meshing methods are applied to two different zones. The Fluid-Domain mesh is generated by using ICEM CFD with blocking technique, a high-quality mesh is created through this method, with the individual mesh elements generated in the form of hexahedral elements. The area of the stationary fluid zone where the rotating fluid zone is situated has a refined mesh near both the distance along the axis and the distance radially from the center. The Fluid-Domain mesh has approximately 1.3 million nodes and elements. Fig. 4a shows the meshing process of the external stationary fluid zone.

The ANSYS meshing tool is used to generate the meshes for the Rotation-Domain - an internal rotating fluid zone. Using this tool is advantageous since it allows for complex geometries to be meshed (Goh, S.C. and Schlüter, J.U., 2016). The Rotation-Domain is segmented into unstructured meshes containing tetrahedral-shaped elements, as shown in Fig. 4 ((b)-(e)). The rotating fluid zone has meshed that become more refined as they get closer to the rotor surface. To capture small flow structures in close proximity to solid walls, the inflation option is employed. The boundary layer is discretized into prism elements, with a growth rate of 1.2 and a maximum of 12 layers, based on similar previous research (Céspedes M., J.F. and Lopez M., O.D., 2019).

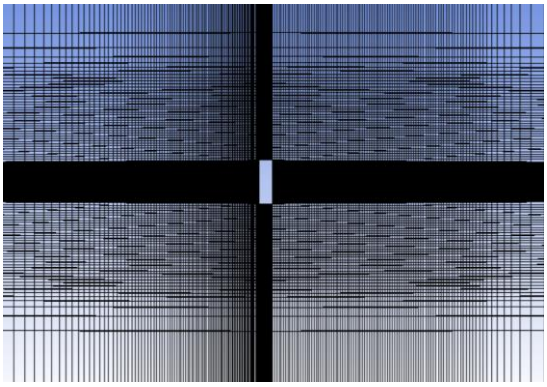

(a)

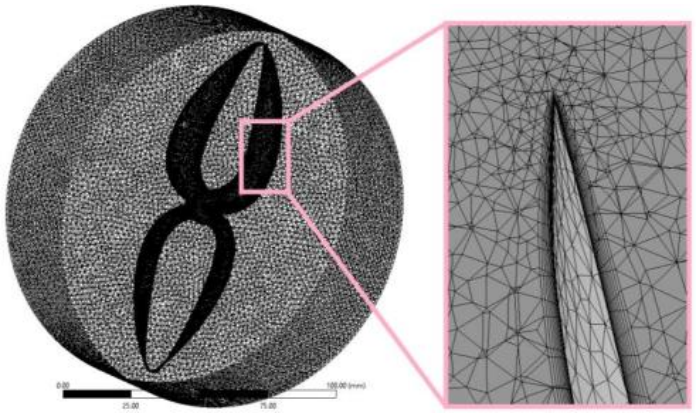

(b)

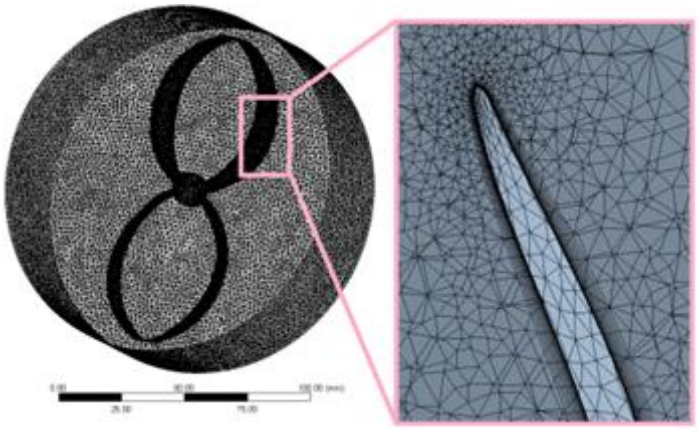

(c)

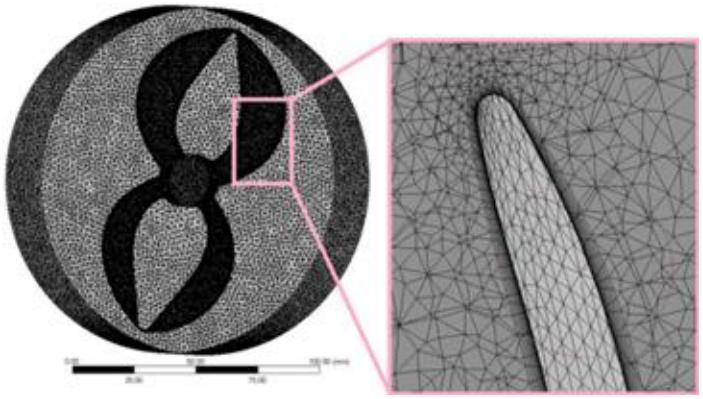

(d)

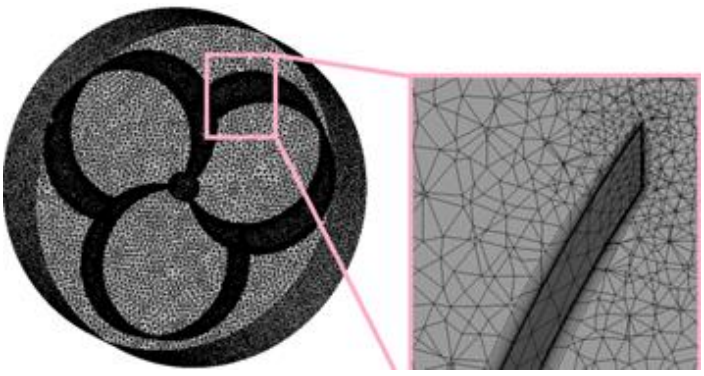

(e)

**Fig. 4.** (a) Middle Z cut plane of The Fluid-Domain mesh is generated by using ICEM CFD; The internal rotating fluid zone mesh and boundary layers section view of the (b) Bi-loop Toroidal Propeller V1 (c) Bi-loop Toroidal Propeller V2 (d) Bi-loop Toroidal Propeller V3 (e) Tri-loop Toroidal Propeller

For a rotational velocity of 20,000 RPM and a chord length equal to 3/4 of the radius position of the propeller, the initial layer thickness is established at 0.005 mm, which corresponds to an average $y^+ = 3.5$. This ensures that the first grid cell falls within a reasonable range of $1 < y^+ < 5$ (Veríssimo, R., 2016; Ewing, P., 2015). Body meshes are also used in the stationary fluid zone to capture most of the simulation's details, along with surface meshes.

To ensure dependable and precise outcomes while optimizing computational resources, a mesh-independence study is conducted to assess the static performance of the propeller. The study evaluated four sets of mesh refinement for four models. The third and fourth Mesh have approximately 4.1 and 5.0 million elements, respectively, on the finer grid side as shown in Fig. 5 for Bi-loop Toroidal V1; 4.6 and 5.7 million elements for V2; 4.1 and 5.3 million elements for V3; 5.1 and 6.4 million elements for Tri-loop Toroidal Propeller. After comparing the results, we have concluded that Mesh 3 is the optimal choice for further calculations. The reason for this choice is that the Thrust values obtained from Mesh 3 are very close to those obtained from Mesh 4, with differences ranging from 0.27% to 1.65%. By opting for Mesh 3 instead of the fourth Mesh, we significantly reduce computational resources while maintaining the accuracy of the results.

### 4.3 Solver Settings

The ANSYS-FLUENT is used to perform numerical simulations, employing a shear stress transport (SST) k-ω turbulence model that includes the best features of k-ε and k-ω models. It provides the k-ε model's free-flow liberation away from the wall, and the k-ω model's accurate expression near the wall boundary layer (Pérez G., A.M., 2017).

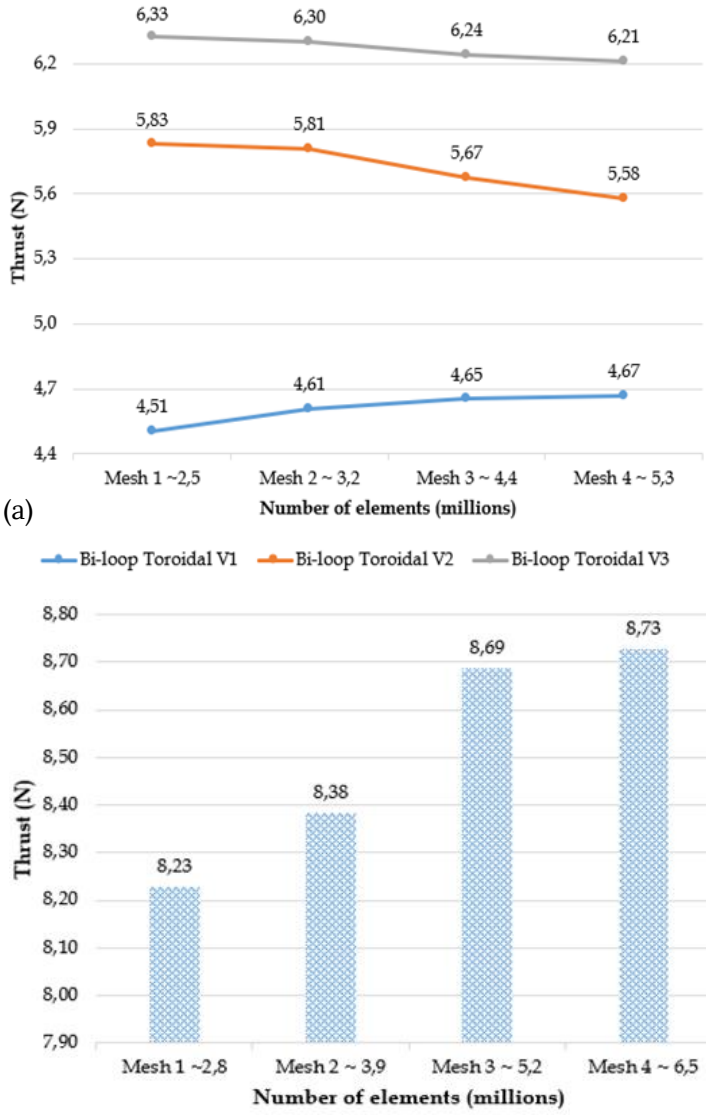


**Fig. 5.** The comparison between thrust and the number of elements for different types of mesh in the mesh independence evaluation (a) Bi-loop Toroidal Propeller V1-2-3 (b) Tri-loop Toroidal Propeller

Based on initial tests with one foil, the Coupled scheme appears to be a suitable option when dealing with a poor mesh that requires the preservation of coupling between velocity and pressure. The sliding mesh interfaces can cause the mesh to become uncoupled, even though the mesh itself is not problematic. To ensure better accuracy compared to the first order, Second Order Upwind is chosen for the pressure and momentum discretization. According to the FLUENT user manual (2019), second order accuracy is recommended when the flow is not aligned with the mesh. In the case of Toroidal Propeller, the mesh is always rotating, thus it is generally misaligned. The First Order Upwind scheme is selected to discretize the turbulent behaviors in RANS simulations, as shown in Table 1. As these behaviors quickly dissipate, they will not travel through many misaligned cells. In the theory section, it is shown how the local behavior of turbulent properties is contained by applying significant damping to their production.

When setting up the acoustic model, a Broadband Noise Source (BNS) Model is used. In Computational Aeroacoustics (CAA), there are various methods to study the acoustical properties of a system. One such method involves applying a BNS model to a steady-state Reynolds-Averaged Navier-Stokes (RANS) Computational Fluid Dynamics (CFD) to learn about the BNS (Wagner, C. et al., 2007). Insight into the source of broadband noise in BNS models can be gained through the use of statistical turbulence quantities obtained from RANS results, semi-empirical correlations, and Lighthill's acoustic analogy. These source terms can help locate and compare noise sources, indicating that BNS models are effective in identifying the primary regions generating noise in a flow domain. Additionally, they provide a way to compare different design variations, allowing for the screening of noisier options and identification of primary noise sources (Wagner, C. et al., 2007; Stanko, T.S. et al., 2008). BNS model parameters are shown in Table 2.

Simulation conducted on a computer with a CPU of Intel(R) Core(TM) i7-9700 processor featuring 8 cores and 8 processors and took a total of 256 hours for 32 cases. Each case took about 8 hours to complete, including 12 mesh independence evaluation cases and 20 optimization simulation cases.

## 5. Results and Discussions

### 5.1 Propeller Performance at Different RPM

Predictions of the propeller's performance in simulations that vary in RPM are shown in the initial findings. Specifically, four models of the Toroidal Propeller were simulated with an RPM-sweep motion, whereby the RPM varies from 10,000 to 20,000. During each timestep, Fluent extracts thrust, velocity, and torque data for each of these models. These parameters, combined with theoretical calculations, yield rotational velocity ($\omega$), power (P), and Power Coefficient (Cp).

The blade geometry changes in the Bi-loop Toroidal Propeller have increased the propeller thrust, with the highest thrust generated by the V3 model at 10,000 rpm. As the rotation speed increases, the difference in thrust between the three Bi-loop models becomes more pronounced, ranging from 1 N to 1.5 N at 20,000 rpm. This is due to the increase in rotor chord length, resulting in a larger aerodynamic area in contact with the air and increasing the camber of the propeller. The Tri-loop Toroidal Propeller generates more thrust than the Bi-loop Toroidal Propeller due to more number of blades, with a significant difference in thrust of about 2.5 N to 4 N.

**Table 1.**Solver Settings

| Parameters | Solution Methods | Model |
|---|---|---|
| Solver | Pressure-Base, Steady, Velocity Formulation - Absolute | |
| Viscous Model | k – ω SST | k: Second Order Upwind<br>ω: First Order Upwind |
| Pressure velocity – coupling | Coupled | |
| Momentum | | Second Order Upwind |
| Pressure | | Second Order |
| Turbulent Kinetic Energy | | First Order Upwind |
| Specific Dissipation Rate | | First Order Upwind |
| Gradient | | Least squares cell based |

Fig. 6 shows that the Bi-loop Toroidal Propeller wing has a wider maximum width in its later version, resulting in an invisible increase in torque.

**Table 2.**BNS Model Parameters

| | |
|---|---|
| Far-Field Density (kg/m$^3$) | 1.225 |
| Far-Field Sound Speed (m/s) | 340 |
| Reference Acoustic Power (W) | 1e-12 |
| Number of Realizations | 200 |
| Number of Fourier Modes | 50 |

The Tri-loop Toroidal Propeller wing performs best at 15,000 - 18,000 rpm and a large difference in torque is observed at 20,000 rpm. Also in Fig. 6, we see a gradual increase in torque and power due to the change in wing geometry in the later version. This change also reduces the power coefficient as the rotation speed increases. Additionally, the Tri-loop Toroidal Propeller shows an optimal power coefficient between 15,000 rpm and 18,000 rpm due to the power coefficient formula (1) where Cp is directly proportional to P and inversely proportional to n3 rotation speed.

### 5.2. Aerodynamic Characteristic Of The Toroidal Propeller

Fig. 7 shows the pressure distribution on the surface of four Toroidal Propeller models that the difference in surface pressure between the body and the edge of the blade creates lift on the wing. A larger pressure difference results in a greater lift force. The three Bi-loop Toroidal models all show that the pressure near the wing tip is larger than the wing hub.

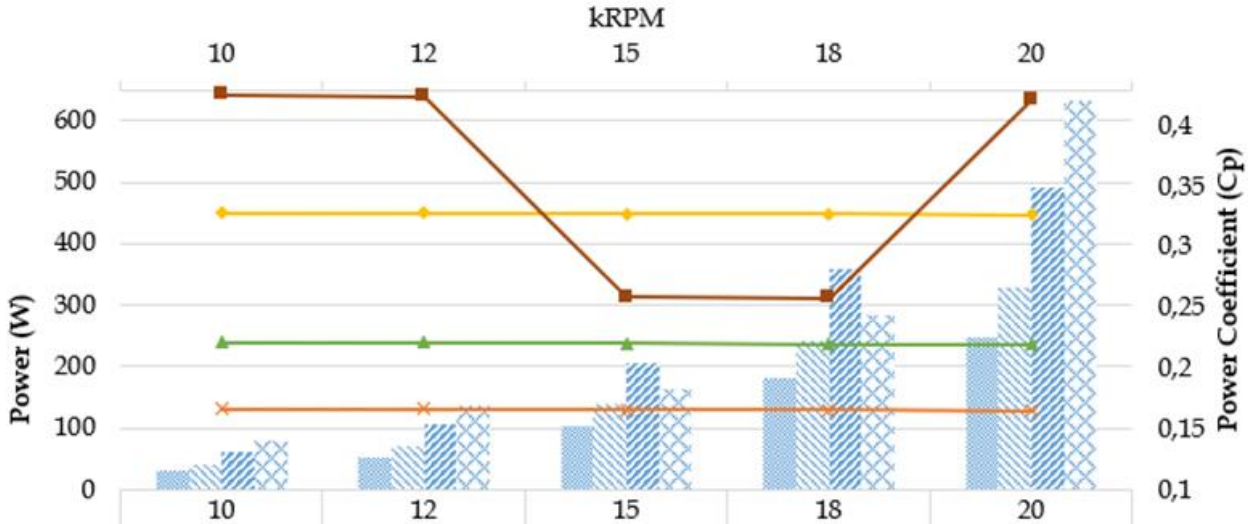


| | 10 | 12 | 15 | 18 | 20 |
|---|---|---|---|---|---|
| Bi-loop V1 | 31,25 | 53,94 | 105,24 | 181,72 | 248,29 |
| Bi-loop V2 | 41,58 | 71,73 | 139,7 | 240,94 | 330,15 |
| Bi-loop V3 | 61,62 | 106,31 | 207,34 | 358,02 | 490,97 |
| Tri-loop | 79,82 | 137,54 | 164 | 282,68 | 632,2 |
| Bi-loop V1 | 0,16679 | 0,16661 | 0,16643 | 0,1663 | 0,16564 |
| Bi-loop V2 | 0,22193 | 0,22155 | 0,22091 | 0,22049 | 0,22025 |
| Bi-loop V3 | 0,32885 | 0,32834 | 0,32787 | 0,32764 | 0,32754 |
| Tri-loop | 0,426 | 0,42479 | 0,25934 | 0,25868 | 0,42176 |

(a)

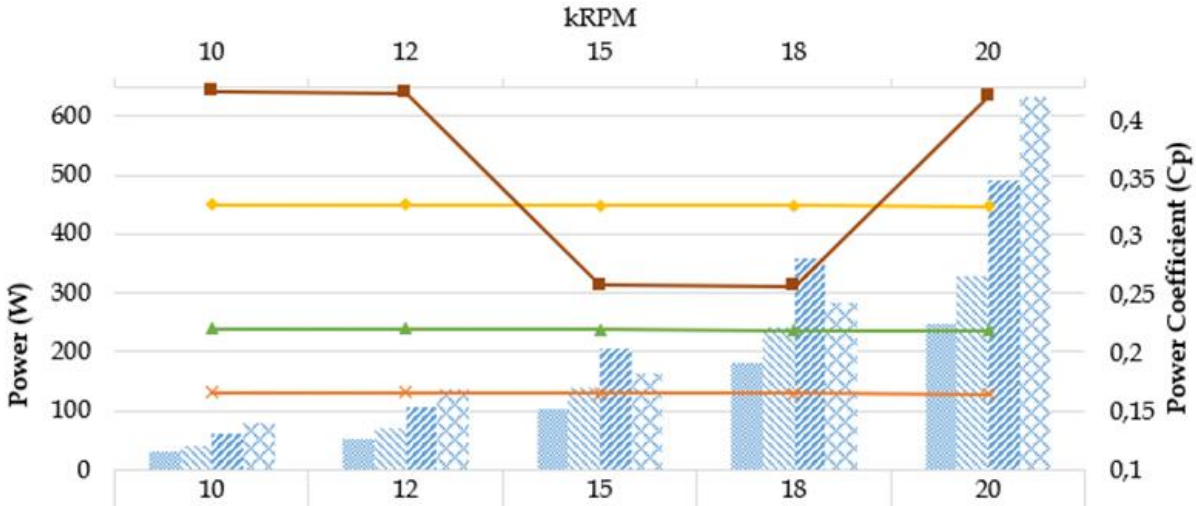


| | 10 | 12 | 15 | 18 | 20 |
|---|---|---|---|---|---|
| Bi-loop V1 | 31,25 | 53,94 | 105,24 | 181,72 | 248,29 |
| Bi-loop V2 | 41,58 | 71,73 | 139,7 | 240,94 | 330,15 |
| Bi-loop V3 | 61,62 | 106,31 | 207,34 | 358,02 | 490,97 |
| Tri-loop | 79,82 | 137,54 | 164 | 282,68 | 632,2 |
| Bi-loop V1 | 0,16679 | 0,16661 | 0,16643 | 0,1663 | 0,16564 |
| Bi-loop V2 | 0,22193 | 0,22155 | 0,22091 | 0,22049 | 0,22025 |
| Bi-loop V3 | 0,32885 | 0,32834 | 0,32787 | 0,32764 | 0,32754 |
| Tri-loop | 0,426 | 0,42479 | 0,25934 | 0,25868 | 0,42176 |

(b)

**Fig. 6.** (a) Thrust (column) versus Torque (line), (b) Power (column) versus Power Coefficient Cp (line) of four Toroidal Propeller models which the RPM changes from 10,000 to 20,000.

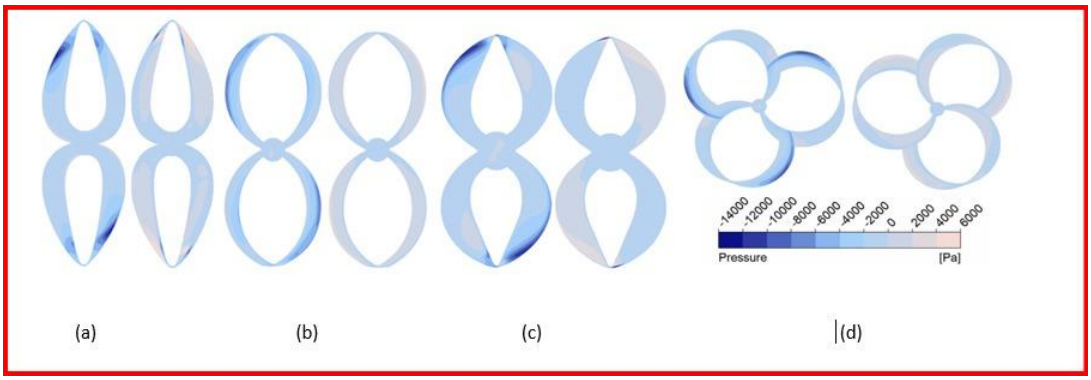


**Fig. 7.** Distributed application on upper surfaces (Right) and lower surfaces (Left) of (a) Bi-loop Toroidal V1 (b) Bi-loop Toroidal V2 (c) Bi-loop Toroidal V3 (d) Tri-loop Toroidal.

Bi-loop Toroidal Propeller V1 shows that the differential pressure distribution is mainly concentrated near the wing tip, whereas Bi-loop Toroidal Propeller V2 and V3 have a more evenly distributed pressure differential over the entire span wing. This partly explains why Bi-loop Toroidal Propeller V2 and V3 give better results in terms of thrust. As for the Tri-loop Toroidal Propeller, due to the uniform wing cross-sections, the pressure concentrated at the tip is not as obvious as the Bi-loop Toroidal Propeller, but the pressure is spread quite evenly over the entire wing surface.

As shown in Fig. 8, the Toroidal Propeller V1 illustrates the presence of a vortex in the flow outside the blade rotation area, at the hub, and at the wing-tip. This phenomenon occurs due to the high intensity of the vortex at the tip of the blade, which influences the outlet stream. Bi-Loop Toroidal Propeller V2 only generates vortex at the wing-tip, but the intensity is insufficient to impact the outflow, unlike V1. Bi-Loop Toroidal Propeller V3, like V2, only generates a vortex at the wing-tip, which is also insufficient to impact outflow too. Through Fig. 8 the flow lines passing through the cross-sections of the four models, we can see that the Bi-loop Toroidal Propeller V1 had vortex losses in the output stream, however V2 and later versions have corrected this. Comparing between V2 and V3, we can see that the flow path coming out of the propeller of Bi-loop V3 is wider

and larger than that of V2, this explains the thrust generated by the V3 blade is much larger than the two versions. previous model. The streamline passing through the Tri-loop Toroidal Propeller is not symmetrical about the x-axis, unlike the previous three Bi-loop Toroidal models. This is because the Tri-loop model has three blades, resulting in an asymmetrical streamline passing through the cross-section of the propeller. The wing-tip vortices of the three Bi-loop Toroidal models have visibly decreased with each improvement. The first model, Bi-loop Toroidal V1, had severe wing-tip vortices that caused damage to the rotor's outer rotation area. This is due, in part, to the thicker loop shape of the wing-tip section. However, V2 and V3 have overcome this problem by having a thinner loop shape that allows for better aerodynamic flow. The Tri-loop Toroidal model has also significantly reduced vortex intensity due to its geometric design since the Tri-loop Toroidal does not really have wing tips, the structural sections of the wings are made even and looped. together, so that the vortex appears at the leading edge and spreads evenly over the surface of the wing.

The wing-tip vortices of the three Bi-loop Toroidal models have visibly decreased with each improvement. The first model, Bi-loop Toroidal V1, had severe wing-tip vortices that caused damage to the rotor's outer rotation area. This is due, in part, to the thicker loop shape of the wing-tip section. However, V2 and V3 have overcome this problem by having a thinner loop shape that allows for better aerodynamic flow. The Tri-loop Toroidal model has also significantly reduced vortex intensity due to its geometric design since the Tri-loop Toroidal does not really have wing tips, the structural sections of the wings are made even and looped. together, so that the vortex appears at the leading edge and spreads evenly over the surface of the wing.

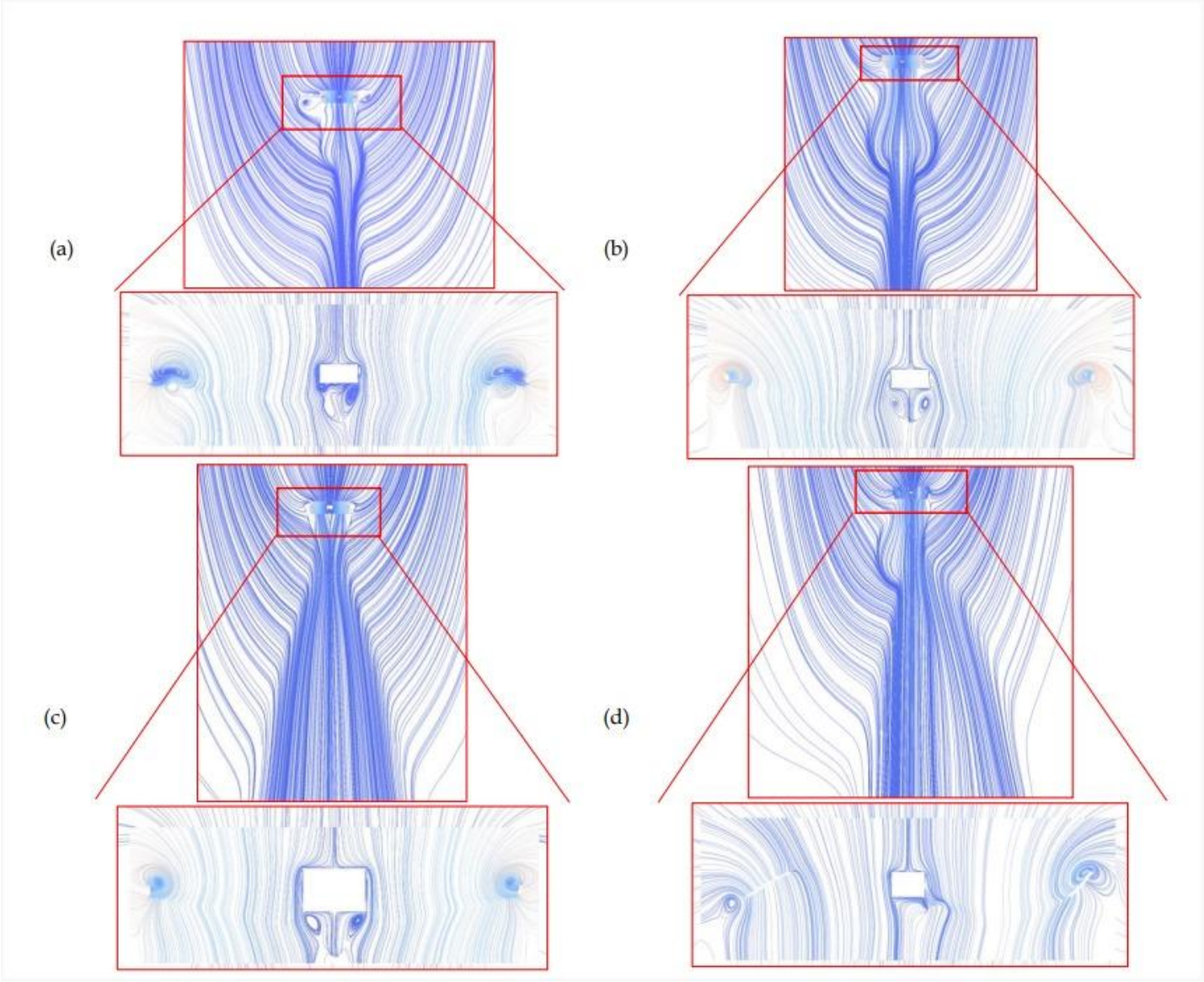


**Fig. 8.** Section of Streamline through (a) Bi-loop Toroidal Propeller V1 (b) Bi-loop Toroidal Propeller V2 (c) Bi-loop Toroidal Propeller V3 (d) Tri-loop Toroidal Propeller

### 5.3 Acoustic Characteristic of the Toroidal Propeller

#### 5.3.1 Qualitative results of Surface Acoustic Power Level (dB) and Acoustic Power Level (dB)

According to previous theoretical predictions, Fig. 9 shows that the noise generated by the propeller around the hub region is relatively small and gradually increases towards the wing-tip, reaching its maximum there. However, the peak surface acoustic power level shows signs of gradually increasing from Bi-loop V1 to V3 models. This can be simply explained by the fact that the acoustic power level on the surface of the blade is greatly influenced by the blade geometry.

As the torque increases, the blade experiences greater friction with the air flow, which leads to the gradual increase in the acoustic power level on the surface of the blade. Fig. 10 illustrates the Acoustic Power Level (APL) power distribution directly related to the propeller output flow. For the Bi-loop Toroidal V1 model, the APL distribution is uneven and concentrated around the wing-tip due to the significant vortices created by the propeller, which cause flow disturbance. However, with the improvements made in the Bi-loop Toroidal V2 model, the APL at the wing-tip has significantly decreased.

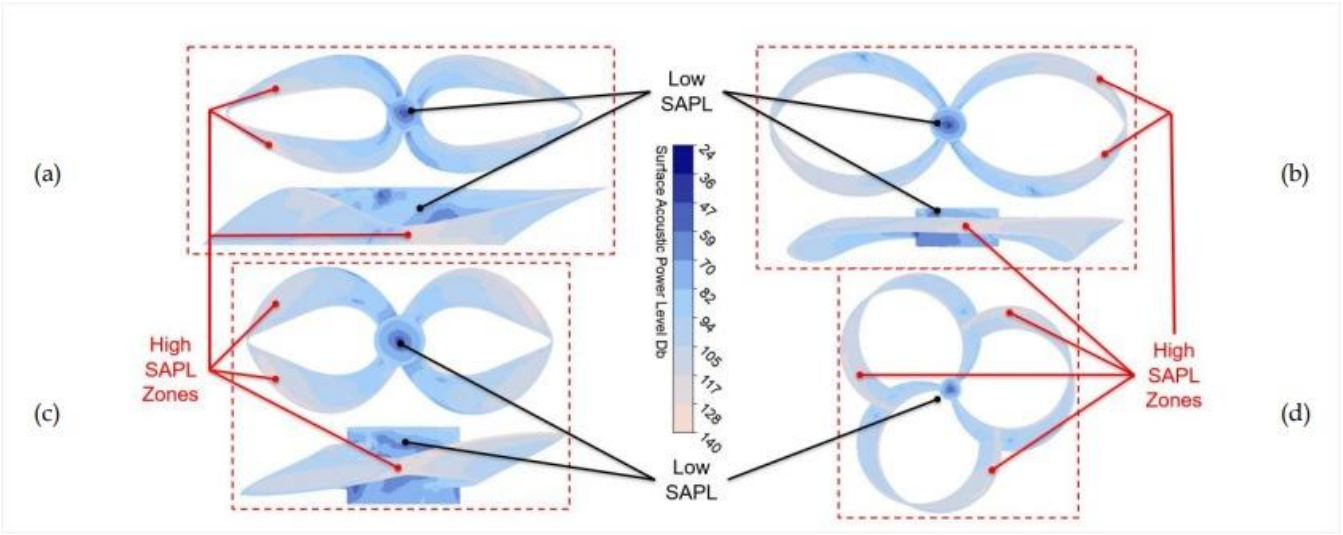


**Fig. 9.** Surface Acoustic Power Level (dB) (Upper surface) of (a) Bi-loop Toroidal V1 (b) Bi-loop Toroidal V2 (c) Bi-loop Toroidal V3 (d) Tri-loop Toroidal

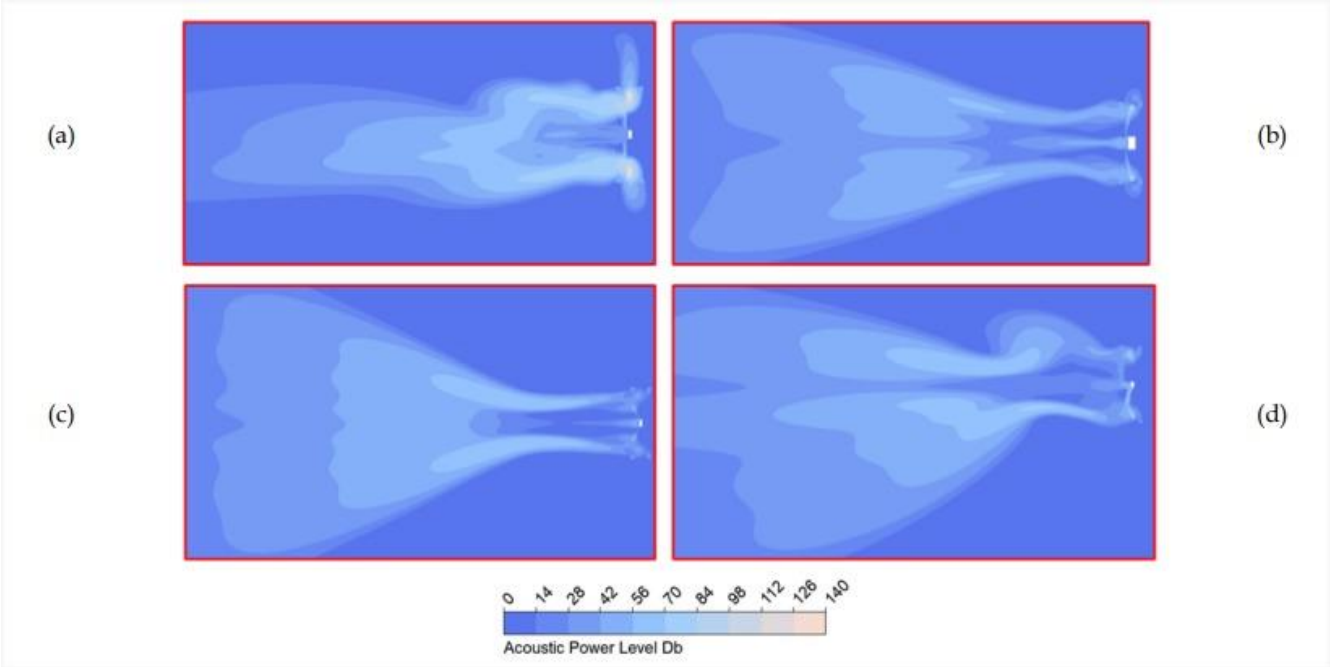


**Fig. 10.** Acoustic Power Level (dB) on outflow of (a) Bi-loop Toroidal V1 (b) Bi-loop Toroidal V2 (c) Bi-loop Toroidal V3 (d) Tri-loop Toroidal

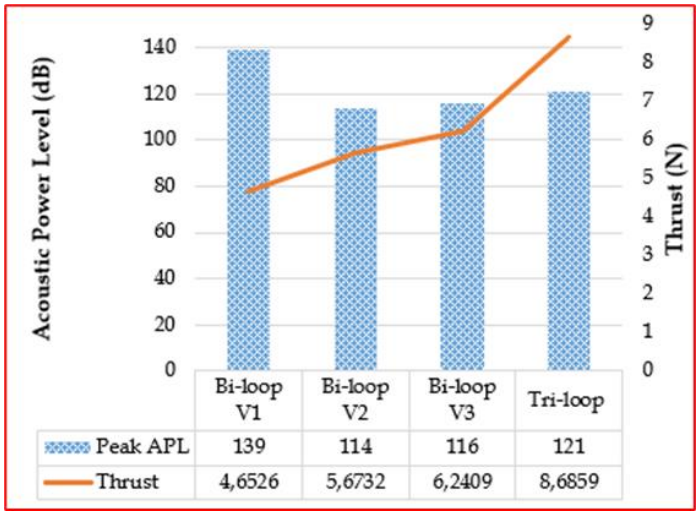


**Fig. 11.** Peak Acoustic Power Level (dB) versus Thrust (N)

### 5.3.2 Quantitative Results of Acoustic Power Level (Db)

In Fig. 11, the APL peak has decreased from 139 dB to 114 dB, indicating an 18% reduction in aerodynamic noise compared to the previous model. Similarly, the Bi-loop Toroidal V3 model has also shown improved noise performance, although there is a slight increase of 116 dB compared to 114 dB of V2 (an increase of 1.7%). In return, it offers more optimal propeller thrust performance, which has increased by 9.13%. As for the Tri-loop Toroidal model, although it generates a slightly larger APL peak than the two Bi-loop Toroidal models V3 and V2 (up 4.13% compared to V3 and up 5.79% compared to V2), its thrust created is the most optimal among all four models. This is due to the increased number of blades, resulting in better thrust performance.

## 6. Conclusions

In this study, four different designs of Toroidal propellers are considered. These designs included a Bi-loop and a Tri-loop Toroidal propellers with different geometric shapes. Two distinct numerical configurations are utilized to evaluate the propeller aerodynamic and acoustic properties. The analysis of performance metrics is based on rotational speed sweeps, while APL data are obtained by using the BNS model, with the propellers spinning at constant RPMs. The results are compared between the four models, and it is shown that the Tri-loop Toroidal propeller provided the most optimal efficiency in terms of both thrust and APL. Among the Bi-loop models, Bi-loop Toroidal V3 produced the most optimal results compared to the two previous Bi-loop Toroidal mockups. This study also confirmed that varying the Toroidal geometries through four versions with different cross-sectional shapes and wing-tips, helped reduce the tip vortices. This stabilized the air flow through the propeller and optimized the thrust and APL generated. Moreover, the numbers in this paper are purely simulation results of Toroidal propeller due to experimental data. Future work will involve experimental studies on the Toroidal propeller model to compare simulation results, optimize the design, and practice different numerical acoustic approaches like the Ffowcs Williams-Hawkings for transient flow solution.

## Acknowledgment

This research is funded by the Ministry of Education and Training (MoET) under Project No. B2023-BKA-11, and the cooperation research between HUST, LQDTU and Viettel Aerospace Institute (VTX).

## CRediT Author Statement

**Vu Xuan-Duc**: Software, Validation, Investigation, Writing- Original draft preparation. **Nguyen Anh-Tuan**: Reviewing and Editing. **Nha Tuong-Linh**: Reviewing and Editing. **Chu Hoang-Quan**: Conceptualization, Methodology, Visualization. **Dinh Cong-Truong**: Data curation, Supervision.

## Nomenclature

| | |
|---|---|
| Cp | : Power coefficient |
| CT | : Thrust coefficient |
| D | : Propeller diameter (m) |
| n | : Rotational velocity (rev.s-1) |
| P | : Power (W) |
| T | : Thrust (N) |
| V | : Forward speed (m.s-1) |
| $\eta$ | : Efficiency |
| $\rho$ | : Air density (kg.m-3) |

## Abbreviations

| | |
|---|---|
| APL | : Acoustic Power Level |
| CFD | : Computational Fluid Dynamic |
| NOB | : Number of Blade |
| RANS | : Reynolds Average Navier-Stokes |
| SAPL | : Surface Acoustic Power Level |

## References

ANSYS. Inc, 2019. ANSYS Fluent User's Manual. Release 2019 R2.

Céspedes M., J.F., Lopez M., O.D., 2019. Simulation and validation of the aerodynamic performance of a quadcopter in hover condition using overset mesh, in: AIAA Aviation 2019 Forum. American Institute of Aeronautics and Astronautics Inc, AIAA.

Chirico, G., Barakos, G.N., Bown, N., 2018. Numerical aeroacoustic analysis of propeller designs. Aeronautical Journal 122, 283–315.

Dantsker, O.D., 2022. Performance Testing of APC Electric Fixed-Blade UAV Propellers, in: AIAA AVIATION 2022 Forum. American Institute of Aeronautics and Astronautics Inc, AIAA.

Demoret, A.C., Wisniewski, C.F., 2019. The impact of a notched leading edge on performance and noise signature of unmanned aerial vehicle propellers, in: AIAA Scitech 2019 Forum. American Institute of Aeronautics and Astronautics Inc, AIAA.

Ewing, P., 2015. Best practices for aerospace aerodynamics, in: STAR East Asia Conference, Singapore.

Garofano-Soldado, A., Sanchez-Cuevas, P.J., ... Ollero, A., 2022. Numerical-experimental evaluation and modelling of aerodynamic ground effect for small-scale tilted propellers at low Reynolds numbers. Aerospace Science and Technology.

Gerr, D., 1989. Propeller Handbook, in: International Marine Publishing.

Goh, S.C., Schlüter, J.U., 2016. Numerical simulation of a Savonius turbine above an infinite-width forward facing step. Wind Engineering 40, 134–147.

Gómez-Iradi, S., Steijl, R., Barakos, G.N., 2009. Development and validation of a cfd technique for the aerodynamic analysis of HAWT. Journal of Solar Energy Engineering, Transactions of the ASME 131, 0310091–03100913

Gur, O., Rosen, A., 2009. Design of a quiet propeller for an electric mini unmanned air vehicle. Journal of Propulsion and Power 25, 717–728.

Kim, D., Lee, Y., ... Park, D., 2021. Aerodynamic analysis and static stability analysis of Manned/unmanned distributed propulsion aircrafts using actuator methods. Journal of Wind Engineering and Industrial Aerodynamics 214.

Klimchenko, V., Baeder, J., 2020. CFD/CSD study of interactional aerodynamics of a coaxial compound helicopter in high-speed forward flight, in: AIAA Scitech 2020 Forum. American Institute of Aeronautics and Astronautics Inc, AIAA.

Krishnamurthy, S., 2021. Remote Psychoacoustic Test for Urban Air Mobility Vehicle Noise Human Response, in: Langley Research Center Hampton, Virginia, United States.

Li, Y., Li, X., ... Zhong, S., 2023. Experimental and numerical investigations on rotor noise in axial descending flight. Physical Review Fluids 8.

Liu, X., Zhao, D., Oo, N.L., 2022. Numerical prediction of the power coefficient improvements of three laterally aligned Savonius wind turbines above a forward-facing step. Journal of Wind Engineering and Industrial Aerodynamics 228.

Marte, J.E., Kurtz, D.W., 1970. A Review of Aerodynamic Noise from Propellers, Rotors, and Lift Fans, JPL Technical Report 32-1462.

MIT Lincoln Laboratory, 2022. Toroidal Propeller.

Misiorowski, M., Gandhi, F., Oberai, A.A., 2019. Computational study on rotor interactional effects for a quadcopter in edgewise flight. AIAA Journal 57, 5309–5319.

Pérez G., A.M., López, O.D., Escobar, J.A., 2017. Computational study of the wake of a quadcopter propeller in hover, in: 23rd AIAA Computational Fluid Dynamics Conference, 2017. American Institute of Aeronautics and Astronautics Inc, AIAA.

Roskam, J., Lan, C., 1997. Airplane Aerodynamics and Performance, in: Airplane Design and Analysis, Design, Analysis and Research Corporation.

Schulz, A., 2023. Development of a Low Noise Drone Propeller Using CFD Simulations. Lund University.

Sebastian, T., Strem, C., 2020. Toroidal Propeller - US Patent (MIT).

Seddon, J., Newman, S., 2011. Basic Helicopter Aerodynamics, Basic Helicopter Aerodynamics. Wiley.

Stanko, T.S., Ingham, D.B., ... Pourkashanian, M., 2008. Computational fluid dynamic prediction of noise from a cold turbulent propane jet, in: Proceedings of the ASME Turbo Expo. pp. 645–652.

Stokkermans, T.C., Van Arnhem, N., ... Veldhuis, L.L.A., 2019. Validation and comparison of RANS propeller modeling methods for tip-mounted applications. AIAA Journal 57, 566–580

Stokkermans, T., Veldhuis, L., ... Eglin, P., 2020. Breakdown of aerodynamic interactions for the lateral rotors on a compound helicopter. Aerospace Science and Technology 101.

Stuermer, A., 2008. Unsteady CFD simulations of contra-rotating propeller propulsion systems, in: 44th AIAA/ASME/SAE/ASEE Joint Propulsion Conference and Exhibit.

Vargas Loureiro, E., Oliveira, N.L., ... de Castro Lemonge,

A.C., 2021. Evaluation of low fidelity and CFD methods for the aerodynamic performance of a small propeller. Aerospace Science and Technology 108.

Veríssimo, R., 2016. Best Practice Guidelines in External Aerodynamics CFD: Applied to Unmanned Aerial Vehicles at Cruise Conditions, in: Doctoral dissertation, Academia da Forc¸a Aérea.

Wagner, C., Hüttl, T., Sagaut, P., 2007. Large-eddy simulation for acoustics, Large-Eddy Simulation for Acoustics. Cambridge University Press.

Wisniewski, C.F., Byerley, A.R., ... Liller, W.R., 2015. The influence of airfoil shape, tip geometry, reynolds number and chord length on small propeller performance and noise, in: 33rd AIAA Applied Aerodynamics Conference. American Institute of Aeronautics and Astronautics Inc, AIAA

Wisniewski, C.F., Byerley, A.R., ... Wisniewski, N., 2015. Experimental evaluation of open propeller aerodynamic performance and aero-acoustic behavior, in: 33rd AIAA Applied Aerodynamics Conference. American Institute of Aeronautics and Astronautics Inc, AIAA.

Wisniewski, C.F., Treuren K.V., 2022. Novel UAS propeller design part I: using an unloaded tip to reduce power requirements and lower generated sound levels for propellers designed for minimum induced drag, in: Proceedings of ASME Turbo Expo 2022 Turbomachinery Technical Conference and Exposition, pp. GT2022-81579.

Wu, Y., Ai, Y.T., ... Chen, Y., 2019. A Novel Aerodynamic Noise Reduction Method Based on Improving Spanwise Blade Shape for Electric Propeller Aircraft. International Journal of Aerospace Engineering 2019.